Helium-4 magnetometers for room-temperature biomedical imaging: toward collective operation and photon-noise limited sensitivity

William Fourcault, Rudy Romain, Gwenael Le Gal, François Bertrand, Vincent Josselin, Matthieu Le Prado, Etienne Labyt, Agustin Palacios-Laloy

Research Article | Vol. 29, No. 10 / 10 May 2021 / Optics Express 14467
Optics EXPRESS

Helium-4 magnetometers for room-temperature biomedical imaging: toward collective operation and photon-noise limited sensitivity

WILLIAM FOURCAULT, RUDY ROMAIN, GWENAEL LE GAL, FRANÇOIS BERTRAND, VINCENT JOSSELIN, MATTHIEU LE PRADO, ETIENNE LABYT, AND AGUSTIN PALACIOS-LALOY*

Univ. Grenoble Alpes, CEA, Leti, F- 38000 Grenoble, France
**agustin.palacioslaloy@cea.fr*

Abstract: Optically-pumped magnetometers constitute a valuable tool for imaging biological magnetic signals without cryogenic cooling. Nowadays, numerous developments are being pursued using alkali-based magnetometers, which have demonstrated excellent sensitivities in the spin-exchange relaxation free (SERF) regime that requires heating to >100 °C. In contrast, metastable helium-4 based magnetometers work at any temperature, which allows a direct contact with the scalp, yielding larger signals and a better patient comfort. However former ^{4}He magnetometers displayed large noises of >200 fT/Hz$^{1/2}$ with 300-Hz bandwidth. We describe here an improved magnetometer reaching a sensitivity better than 50 fT/Hz$^{1/2}$, nearly the photon shot noise limit, with a bandwidth of 2 kHz. Like other zero-field atomic magnetometers, these magnetometers can be operated in closed-loop architecture reaching several hundredths nT of dynamic range. A small array of 4 magnetometers operating in a closed loop has been tested with a successful correction of the cross-talks.

1. Introduction

Biomagnetic imaging is foreseen as a very promising technique for clinical research on human brain [1], heart [2], fetal organs [3] and nerves [4], as well as for animals [5] and even plants [6]. The development of optically pumped magnetometers (OPM) has opened the possibility of performing magnetoencephalography (MEG) without cryogeny, which paves the way to wearable MEG [7].

Most of the current OPM are based on optical pumping of alkali atoms –mainly rubidium and cesium– with circularly polarized light. Some of these magnetometers are able to operate at room temperature, with comparatively low densities of alkali [5,8]. However the very best sensitivities are reached in the so-called spin-exchange relaxation free (SERF) regime which requires heating the cell above 100°C. Excellent sensitivities have been reported in this regime, down to 0.54 fT/Hz$^{1/2}$ [9] on lab tests and around 10 fT/Hz$^{1/2}$ in commercial sensors [10]. Magnetocardiography (MCG) for instance has been addressed with both kind of sensors: scalar cesium Mx magnetometers operating at room temperature [11] and rubidium SERF magnetometers [12].

Alkali magnetometers operating in the SERF regime show some practical drawbacks: for biomedical measurements the high temperature of the cell requires adding thermal insulation between the body and the sensitive element. Also since T_2 dephasing times are quite long in this regime, the magnetometer bandwidth is narrow [13]. In addition most magnetometers operate in open loop, which yields a narrow dynamic range of a few nT, and increased sensitivity to spurious effects.

This work presents a sensor based on an alternative sensitive species: helium-4 atoms, in their $F = 1$ metastable level, which can be significantly populated by using a low-intensity

#420031 https://doi.org/10.1364/OE.420031
Journal © 2021 Received 19 Jan 2021; revised 5 Mar 2021; accepted 15 Mar 2021; published 28 Apr 2021

Optics EXPRESS

radio-frequency discharge of only a few mW. This species has been used for a long time in scalar magnetometers for space and magnetic anomaly detection applications [14–16]. Since helium is a gas at room temperature no heating of the sensitive element is needed. This allows operating the magnetometers at any temperature, and notably in direct contact with patient skin or scalp without any thermal discomfort.

Clinical proof-of-concept measurements of magnetocardiography and MEG have been carried out a few years ago [17,18] with helium magnetometers. The preliminary sensors used in these works were however cumbersome and suffered from large technical noises which raised their intrinsic noise above 200 fT/Hz$^{1/2}$.

We report here the development and test of a new generation of helium magnetometers for biomedical measurements. The new sensor scheme (described in Sec. 2) allows a particularly compact configuration, which is made possible thanks to the specific kind of pumping used. Thanks to numerous improvements (outlined in Sec. 3) the intrinsic noise of the sensor has been reduced below 50 fT/Hz$^{1/2}$, in the close vicinity of the photon noise of the probe laser. Closed-loop operation (which is described in Sec. 4) where the local magnetic field is continuously cancelled thanks to 3-axis compensation coils, allows a virtually-unlimited dynamic range. The operation of an array of 4 magnetometers placed side-by-side and its cross-talks are described in Sec. 5. We finally discuss (in Sec. 6) the current perspectives for helium-4 low field magnetometers.

2. Magnetometer configuration

The sensitive species used in our magnetometers is the metastable 2^3S_1 level of helium-4. This level can be populated by a high-frequency (HF, between 10-20 MHz) discharge, which brings a significant population (typically of a few 10^{11} cm^{-3}) to the longest-lived level: the metastable, while keeping relaxation times slightly below 1 ms [19]. This level can be optically pumped using the D_0 ($2^3S_1 \rightarrow 2^3P_0$, $F = 1 \rightarrow F' = 0$) transition at 1083.2 nm wavelength [20], which has the advantage of being insensitive to collisional mixing on the excited state.

Unlike most OPM where the pumping light is circularly polarized, our magnetometers are pumped with linearly polarized light. This kind of pumping creates a spin polarization called alignment, which corresponds to a quadrupole magnetic moment of the atomic ensemble [21,22]. This choice has several advantages. The first one is that the characteristic direction of alignment follows the one of the light polarization $\vec{E}$ and not of its propagation $\vec{k}$. This allows sensing the component of the magnetic field radial to the head, which is the most significant in MEG, while pump beams propagate also radially. In this configuration the only optical element needed is a mirror on the bottom of each cell, which does not enlarge the footprint of the sensor. This is in contrast with configurations based on atomic orientation which either require an optical element (like a collimator or a prism) to be placed on a side of the cell, which enlarges the footprint of each individual sensor [23,24], or can only measure the components of the field tangential to the head [25,26].

Another advantage is that the vector light shifts are replaced by tensor light-shifts which have a lower impact on measurement [27]. Moreover, for metastable helium, the choice of alignment over orientation causes no reduction of the sensitivity. Indeed, the reduction of a factor 2 in the amplitude of the optical signals is compensated by the two-times faster precession of alignment, yielding equivalent slopes of the photo-detection signals [28].

There are several configurations of null-field magnetometers using radio-frequency (RF) fields. The first and simplest case is a single-axis parametric resonance magnetometer, where a single oscillating RF field allows measuring the component of the magnetic field which is parallel to it [28,29]. The first characterizations performed below are made in this single-axis configuration.

A second possibility consists in adding a second oscillating RF field, orthogonal to the first one but at a different frequency. The physics of this configuration can be studied in the dressed-atom formalism [28,29]. This scheme allows obtaining the two components of the magnetic field

Optics EXPRESS

orthogonal to light polarization with a given sensitivity, and the third one with a worse one (typically by a factor 6). Most of the experiments reported below are performed in this tri-axial scheme.

A third configuration, which is not used in the current work, consists in using rotating RF fields [10,30] for getting two or three components of the magnetic field.

An outline of our sensors is presented in Fig. 1. A 1-cm long and 1-cm diameter glass cell filled with just 10 Torr of ultra-pure helium-4 is set on the bottom of the sensor, its outer part being about 1 mm apart of the patient skin. Electrodes set on each side of the cell allow to excite a HF discharge at 17.4 MHz, consuming 17 mW power. A laser beam tuned to D_0 transition of helium is carried by an optical fiber, polarized, and collimated by a converging lens. The bottom of the glass cell is coated with a dielectric mirror which reflects the beam, which thanks to the same lens, converges and is photo-detected by an InGaAs photo-diode integrated in the sensor package. The bottom of the sensor is surrounded by small 3-axis Helmholtz coils which are used for applying both the RF fields, of 770 nT amplitude at 40 kHz along the y axis, and 175 nT at 9 kHz along the x axis, and the compensation fields. The latter allow closed-loop operation that will be described below. All the elements are maintained together by a 3D printed mount made from a photosensitive resin. The current sensor footprint is 2×2 cm^2, although some optimization should allow to reduce it by at least 25% without changing the position of the functional parts of the sensor.

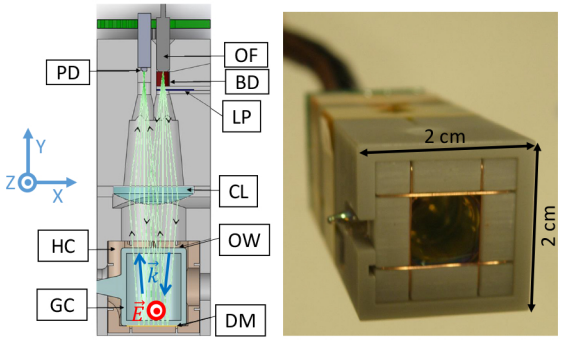

Fig. 1. Helium-4 compact OPM. (a) Cross-section showing the functional parts. (b) Photograph showing the bottom of the sensor and its footprint size. LP: linear polarizer. OF: optical fiber. PD: InGaAs photodiode. CL: converging lens. OW: optical window. DM: dielectric mirror. GC: glass cell containing helium-4. HC: triaxial Helmholtz coils. BD: beam divergence.

3. Noise and bandwidth characterization of a single OPM

The main issue with former helium-4 OPM was their very high intrinsic noise [17,18]. This noise was due to several causes: the fiber laser that was used had a relative intensity noise (RIN) more than 10 dB above the photon noise. Also the materials surrounding the helium cell were not perfectly amagnetic and created excess magnetic noise. A full rework of the sensor design, notably its optical configuration, as well as the replacement of the laser with a model with a lower RIN allowed a substantial reduction of the intrinsic magnetometer noise.

The intrinsic noise of a typical sensor in the open-loop single axis configuration (only one RF on) is presented in Fig. 2(b). For characterizing this noise the sensor is set in the center of a five-layer mu-metal cylindrical magnetic shielding of 60-cm inner diameter and 1-m length, with residual field of 11 nT along its axial direction and <5 nT along transverse directions. A pigtailed laser is sent through a polarization maintaining fiber. An optical attenuator allows controlling the

Optics EXPRESS

optical power sent to the magnetometer. The photo-detection signal is brought through a coaxial cable out of the magnetic shielding, input to a trans-impedance amplifier. The resulting signal is demodulated at the RF frequency (40 kHz) by a commercial lock-in amplifier (SRS-865A), and the result is stored in a computer for treatment. A reference signal at 70 Hz, with a calibrated amplitude of 100 pT rms is applied along the sensitive axis thanks to a large (30 cm) 3-axis coils with the magnetometer placed in the center. By choosing a 1 Hz resolution bandwidth in the spectrum analyzer, this reference allows a real-time calibration of the sensor open-loop transfer function during the intrinsic noise characterization.

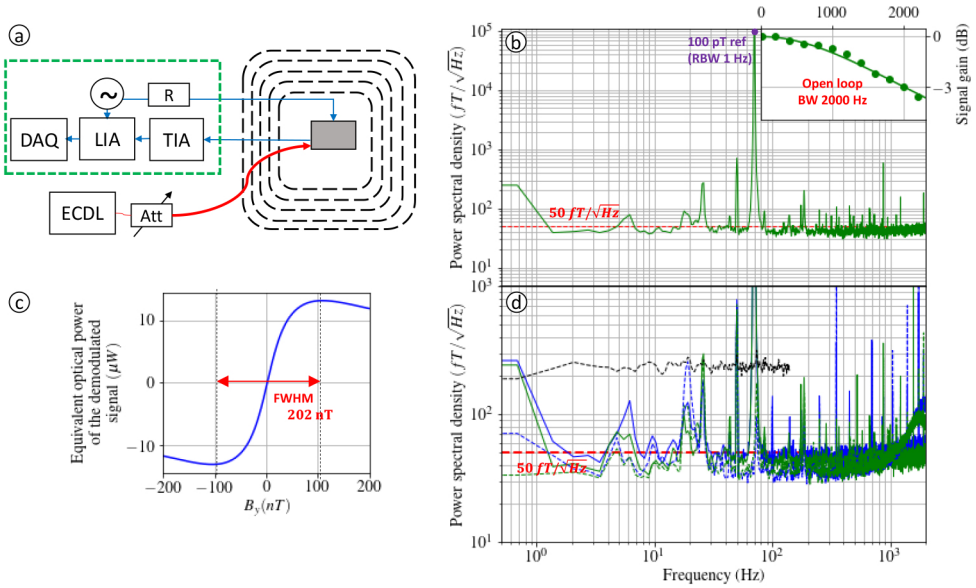

Fig. 2. Performance of our helium-4 OPM. (a) Setup for the characterization of the intrinsic noise. The blue paths correspond to electrical signals and the red ones to optical fibers. The black dashed lines are mu-metal magnetic shield layers. Green dashed line encloses the electronic functions that can be handled by the discrete devices shown inside, or by sub-functions in our proprietary digital electronics board. (b) Intrinsic noise and bandwidth of the OPM in the single-axis open-loop configuration normalized by the bandwidth shown in the inset. (c) Open-loop response of the photo-current demodulated at 40 kHz with respect to the B_y component of the magnetic field in the single-axis configuration. (d) Intrinsic noises of the magnetometer in the tri-axial configuration in open-loop (solid lines, normalized with their respective bandwidths) and closed-loop (dashed lines): x (blue), y (green) and z (black). ECDL: external cavity diode laser. Att: variable optical attenuator. TIA: trans-impedance amplifier. LIA: lock-in amplifier. DAQ: data acquisition card. R: resistor network.

The measured intrinsic noise is lower than 50 fT/Hz$^{1/2}$, and is currently limited by the optical noise of the laser. At 40 kHz we measured this noise to be 1.6 ± 0.5 dB above the photon shot noise.

The sensor bandwidth was also measured by injecting a reference signal in the coil and measuring the output of the magnetometer while changing the reference signal frequency. The frequency response measurement is shown as inset in Fig. 2(b): it matches a first order low pass filter, with 2-kHz bandwidth at -3 dB.

Optics EXPRESS

4. Closed-loop operation

One of the specific features of our OPM is the closed-loop operation mode, consisting in continuously cancelling the three components of the magnetic field of each sensor by applying an opposite compensation field $\vec{B}_c$ with the 3-axis Helmholtz coils. Closed-loop operation has been applied to other magnetometer schemes: RF magnetometers [31] and gradiometers [32].

To perform this real-time cancellation of the three magnetic field components, we use a rather different scheme, sketched on Fig. 3, containing an integrator in order to cancel the static error, and achieving better accuracy of the field cancellation. The closed-loop transfer function $T(s)$ of this scheme can be written:

$$\frac{I_{m,i}}{B_{0,i}} = T(s) = \frac{1}{K_c} \frac{1}{1 + \frac{s}{K_c K_i K_O}} \tag{1}$$

with $B_{0,i}$ the component i ($i \in \{x, y, z\}$) of the pre-existing magnetic field, $I_{m,i}$ the current sent to the compensation coils for the i axis, s the Laplace variable and K_c, K_i and K_O the gains of the coil driver, the integrator and the OPM respectively.

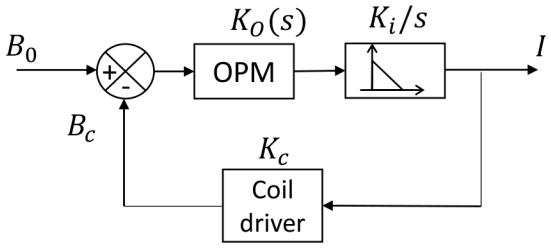

Fig. 3. Schematic of the control system used to generate the compensation field for each component of the magnetic field. The component $i \in \{x, y, z\}$ of the preexisting magnetic field $B_{0,i}$ is superimposed with the component i of the compensation field, and the resulting field is the one observed by the OPM, which is characterized by a gain K_O. The output is sent to an integrator with gain K_i yielding the compensation current $I_{m,i}$, which is fed back to the driver of the compensation coils, which show a gain K_c. This compensation current is proportional to the measured component of the field along the axis i which is noted $B_{m,i}$

If we neglect the low-pass filtering by the atomic response, i.e. we consider a constant $K_O(s)$, the transfer function $T(s)$ is a low pass filter with static transfer coefficient K_c^{-1} and time constant $(K_c K_i K_O)^{-1}$. Therefore fluctuations in the amplitude of the OPM transfer function K_O, due for instance to changes in laser or plasma intensity have no impact on the measured value, but just cause fluctuations of the closed-loop bandwidth, which have a minor impact on recordings, specially when the bandwidth is large. This is an important advantage since it eliminates the need for calibration except for the transfer function of the 3-axis Helmholtz coils surrounding the helium cell. An even more important advantage consists in the possibility of broadening the dynamic range well above the magnetic line-width of the atoms. In our preliminary electronic boards ±300 nT have been achieved, but this can be improved further, the only limit being the technical compromise between the range of the coil drivers and their technical noise [33,34].

The intrinsic noise of our magnetometer operating in the closed-loop tri-axial mode is shown in Fig. 2(d). No additional noise as compared to the open-loop configuration is observed and the sensitivity is still better than 50 fT/Hz$^{1/2}$. The raise of the noise floor observed at high frequencies comes from a non-optimal choice of the integrator gain causing a reduction of the closed-loop bandwidth down to 1350 Hz.

Optics EXPRESS

5. Four-magnetometer array

However, closed-loop operation has also some unwanted consequences due to the cross-talks that unavoidably exist between the coils of closely-packed sensors. Due to these cross-talks there is a difference between the magnetic field which pre-existed before the closed-loop array is started, and the readings of the sensors. This difference, if it is not corrected, perturbs the spatial distribution of the measured magnetic fields, which could yield errors in the source localisation algorithms like the ones used, for instance, for finding the epilepto-genetic areas in the brain [35].

However, this problem can be solved by appropriate post-processing as far as the cross-talks are appropriately characterized. Indeed the field at each magnetometer is the result of the preexisting field, the magnetometer back-action, but also the back-action of the neighbor magnetometers. For each component (x, y or z) of the magnetic field the situation when closed-loop operation is active, and therefore the total field at each magnetometer is null, can be modelled as the vector equation [34,36]:

$$\begin{pmatrix} B_1 \\ B_2 \\ \vdots \\ B_N \end{pmatrix} - \begin{bmatrix} \frac{\partial B_1}{\partial I_1} & \frac{\partial B_1}{\partial I_2} & \cdots & \frac{\partial B_1}{\partial I_N} \\ \frac{\partial B_2}{\partial I_1} & \frac{\partial B_2}{\partial I_2} & \cdots & \frac{\partial B_2}{\partial I_N} \\ \vdots & \vdots & \ddots & \vdots \\ \frac{\partial B_N}{\partial I_1} & \frac{\partial B_N}{\partial I_2} & \cdots & \frac{\partial B_N}{\partial I_N} \end{bmatrix} \begin{pmatrix} I_1 \\ I_2 \\ \vdots \\ I_N \end{pmatrix} = \begin{pmatrix} 0 \\ 0 \\ \vdots \\ 0 \end{pmatrix} \tag{2}$$

Therefore the pre-existing field (B_i) can be deduced from the I_i currents in the sensors as far as the square matrix is known. This matrix can either be estimated from Biot-Savart calculations, or experimentally calibrated as described hereafter.

The combination of cross-talks between adjacent magnetometers with closed-loop multi-axis operation has to be carefully considered to avoid any instabilities and be able to correct the recordings. As a first test to probe the possibility of operating several magnetometers in closed-loop in the presence of cross-talks we have manufactured an array of four magnetometers, set side-by-side with only 2-mm spacing, a rather unfavorable situation as compared to real MEG. This setup is shown in Fig. 4.

After turning the laser on, we started the compensation electronics of each magnetometer sequentially. No instabilities were observed: the magnetometers only showed small deviations from their initial values when starting the electronics of their neighbors. We applied an offset magnetic field using the large 3-axis cubic coil shown in Fig. 4, which was recorded by all the magnetometers of the array, until reaching the limit of their dynamic range, which was around ±250 nT.

We then calibrated the cross-talk 12×12 matrix $\mathbf{A}$, with elements:

$$A_{i,j} = (\partial B_j/\partial I_i)/(\partial B_i/\partial I_i) \tag{3}$$

A first attempt to do so using open-loop operation of all the network produced rather strange results due to the presence of crossed-axes terms which are expected if the magnetic field is not perfectly cancelled along all the axes [37]. We thus used a variant of this procedure, similar to the one described in [36], which consists in setting sinusoidal reference signals in all the coils of the array at the same time but different frequencies, while keeping only one magnetometer in closed loop at each time, this magnetometer being the only one being read. This procedure, which is being patented, resulted in couplings which are in good agreement with the calculations made from Biot-Savart law considering the actual positions of the sensors as set by the plastic mount that holds the four magnetometers. All but one of the coupling coefficients measured in such way are in 10% range of their theoretical predictions, this 10% uncertainty resulting mainly from the uncertainty of the probe position in the holder. Only one coefficient deduced from a

Optics EXPRESS

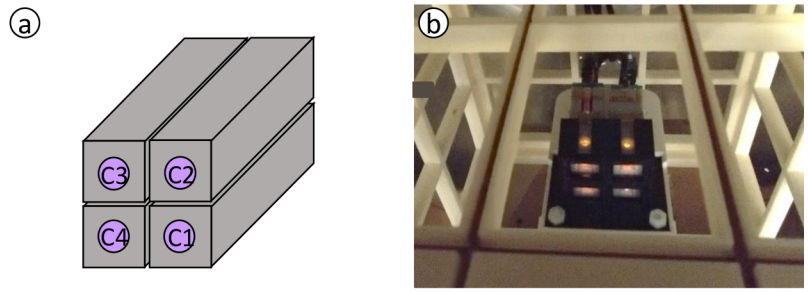

c

		C1			C2			C3			C4		
		x	y	z	x	y	z	x	y	z	x	y	z
C1	x	100,0%	0,0%	-0,3%	0,0%	0,0%	3,1%	0,6%	-0,1%	1,7%	0,2%	-0,2%	-6,3%
	y	0,0%	100,0%	0,0%	-0,4%	-2,8%	-0,1%	-0,1%	-1,1%	-0,1%	0,0%	-3,0%	0,3%
	z	0,0%	0,0%	100,0%	6,1%	-0,3%	0,0%	1,8%	-0,1%	0,6%	-3,4%	0,0%	-0,2%
C2	x	0,1%	-0,5%	6,3%	100,0%	0,0%	-0,1%	0,0%	-0,1%	-3,2%	0,6%	-0,1%	1,9%
	y	0,0%	-2,9%	-0,6%	0,0%	100,0%	0,0%	-0,1%	-3,0%	0,0%	0,0%	-1,1%	-0,1%
	z	3,3%	0,0%	0,0%	0,0%	0,0%	100,0%	-6,2%	0,0%	0,1%	1,8%	-0,1%	0,7%
C3	x	0,6%	-0,1%	1,8%	-0,1%	-0,1%	-6,2%	100,0%	0,0%	-2,1%	0,0%	-0,1%	3,5%
	y	-0,1%	-1,1%	-0,1%	-0,1%	-2,9%	0,3%	0,0%	100,0%	0,1%	-0,2%	-3,1%	0,0%
	z	1,8%	-0,1%	0,6%	-3,3%	0,1%	0,2%	0,1%	0,0%	100,0%	6,5%	-0,3%	0,0%
C4	x	-0,1%	0,0%	-3,4%	0,6%	-0,1%	1,7%	0,0%	-0,2%	6,2%	100,0%	0,0%	-0,1%
	y	-0,3%	-3,0%	0,1%	-0,1%	-1,1%	-0,1%	0,0%	-3,0%	-0,3%	0,0%	100,0%	0,0%
	z	-6,3%	0,3%	0,1%	1,8%	0,0%	0,6%	3,3%	0,0%	-0,2%	0,0%	0,0%	100,0%

Fig. 4. Four magnetometer array. (a) Schematic drawing of the four magnetometer relative placement. The magnetometer footprint is 2 cm × 2 cm and the spacing between adjacent magnetometers is 2 mm. (b) Photograph of the magnetometer array installed inside a set of 3-axis coils, itself inside a 5-layer magnetic shielding. (c) Matrix **A** of the relative couplings between the magnetometers: each line corresponds to a coil creating a reference magnetic field, each column to a magnetometer measuring all the signals in closed-loop mode. 143 of these couplings (in green) comply with the theoretical predictions, only one (in orange) shows substantial disagreement.

measurement of the least resolved axes of the third sensor (C3) seems wrong: the reason of this small disagreement is currently being studied. Otherwise the procedure used for characterizing the couplings seems to be appropriate and should allow a post-treatment correction of the cross-talks as discussed above.

In the very same way as compensation signals couple one magnetometer to another, so do the RF fields. Unless the magnetometers are placed in a very particular configuration this will not only cause a variation of the RF amplitudes [38], but more importantly a spurious change in the RF directions, which can be more problematic because it controls the direction of sensitive axes of the magnetometer. Efforts have been made to develop magnetometers requiring no RF, which are therefore immune to these effects [39]. However, a more pragmatic solution could be to correct these misalignements by an appropriate data processing, taking advantage of the knowledge of the DC couplings.

6. Perspectives of helium-4 magnetometer development

Although their intrinsic noise is still worse than alkali-based OPM, helium-4 OPM have practical advantages, notably the possibility of operating at room temperature, without any cooling or heating, and have undergone important progress these last years. Larger arrays of helium-4 OPM are being developed and should allow addressing clinical applications where the combination of a large bandwidth and a greater proximity to the sources brings a substantial advantage.

Funding. Agence Nationale de la Recherche (Carnot CEA LETI grant).

Optics EXPRESS

Acknowledgments. We want to acknowledge interesting discussions with Pierre-Jean Nacher, Jean-Michel Léger, Hervé Gilles, Serge Gidon, Yoanna Nowicki, François Beato, Thomas Jager and Sophie Morales, and cell filling by François Alcouffe.

Disclosures. The authors declare no conflicts of interest.

References

1. S. Supek and C. J. Aine, eds., *Magnetoencephalography: From Signals to Dynamic Cortical Networks* (Springer-Verlag, Berlin Heidelberg, 2014).
2. A. J. Camm, R. Henderson, D. Brisinda, R. Body, R. G. Charles, B. Varcoe, and R. Fenici, "Clinical utility of magnetocardiography in cardiology for the detection of myocardial ischemia," J. Electrocardiol. **57**, 10–17 (2019).
3. I. A. Sulai, Z. J. DeLand, M. D. Bulatowicz, C. P. Wahl, R. T. Wakai, and T. G. Walker, "Characterizing atomic magnetic gradiometers for fetal magnetocardiography," Rev. Sci. Instrum. **90**(8), 085003 (2019).
4. P. J. Broser, S. Knappe, D. Kajal, N. Noury, O. Alem, V. Shah, and C. Braun, "Optically pumped magnetometers for magneto-myography to study the innervation of the hand," *IEEE Transactions on Neural Systems and Rehabilitation Engineering* p. 1 (2018).
5. K. Jensen, M. A. Skarsfeldt, H. Stærkind, J. Arnbak, M. V. Balabas, S.-P. Olesen, B. H. Bentzen, and E. S. Polzik, "Magnetocardiography on an isolated animal heart with a room-temperature optically pumped magnetometer," Sci. Rep. **8**(1), 16218–9 (2018).
6. E. Corsini, V. Acosta, N. Baddour, J. Higbie, B. Lester, P. Licht, B. Patton, M. Prouty, and D. Budker, "Search for plant biomagnetism with a sensitive atomic magnetometer," J. Appl. Phys. **109**(7), 074701 (2011).
7. E. Boto, N. Holmes, J. Leggett, G. Roberts, V. Shah, S. S. Meyer, L. D. Muñoz, K. J. Mullinger, T. M. Tierney, S. Bestmann, G. R. Barnes, R. Bowtell, and M. J. Brookes, "Moving magnetoencephalography towards real-world applications with a wearable system," Nature **555**(7698), 657–661 (2018).
8. S. Groeger, G. Bison, J.-L. Schenker, R. Wynands, and A. Weis, "A high-sensitivity laser-pumped Mx magnetometer," Eur. Phys. J. D **38**(2), 239–247 (2006).
9. I. K. Kominis, T. W. Kornack, J. C. Allred, and M. V. Romalis, "A subfemtotesla multichannel atomic magnetometer," Nature **422**(6932), 596–599 (2003).
10. O. Alem, R. Mhaskar, R. Jiménez-Martínez, D. Sheng, J. LeBlanc, L. Trahms, T. Sander, J. Kitching, and S. Knappe, "Magnetic field imaging with microfabricated optically-pumped magnetometers," Opt. Express **25**(7), 7849–7858 (2017).
11. G. Lembke, S. N. Erné, H. Nowak, B. Menhorn, A. Pasquarelli, and G. Bison, "Optical multichannel room temperature magnetic field imaging system for clinical application," Biomed. Opt. Express **5**(3), 876 (2014).
12. Y. J. Kim, I. Savukov, and S. Newman, "Magnetocardiography with a 16-channel fiber-coupled single-cell Rb optically pumped magnetometer," Appl. Phys. Lett. **114**(14), 143702 (2019).
13. J. C. Allred, R. N. Lyman, T. W. Kornack, and M. V. Romalis, "High-Sensitivity Atomic Magnetometer Unaffected by Spin-Exchange Relaxation," Phys. Rev. Lett. **89**(13), 130801 (2002).
14. D. D. McGregor, "High-sensitivity helium resonance magnetometers," Rev. Sci. Instrum. **58**(6), 1067–1076 (1987).
15. J.-M. Leger, F. Bertrand, T. Jager, M. Le Prado, I. Fratter, and J.-C. Lalaurie, "Swarm Absolute Scalar and Vector Magnetometer Based on Helium 4 Optical Pumping," Procedia Chem. **1**(1), 634–637 (2009).
16. G. Lieb, T. Jager, A. Palacios-Laloy, and H. Gilles, "All-optical isotropic scalar 4He magnetometer based on atomic alignment," Rev. Sci. Instrum. **90**(7), 075104 (2019).
17. S. Morales, M. C. Corsi, W. Fourcault, F. Bertrand, G. Cauffet, C. Gobbo, F. Alcouffe, F. Lenouvel, M. L. Prado, F. Berger, G. Vanzetto, and E. Labyt, "Magnetocardiography measurements with 4He vector optically pumped magnetometers at room temperature," Phys. Med. Biol. **62**(18), 7267–7279 (2017).
18. E. Labyt, M. Corsi, W. Fourcault, A. Palacios Laloy, F. Bertrand, F. Lenouvel, G. Cauffet, M. L. Prado, F. Berger, and S. Morales, "Magnetoencephalography With Optically Pumped 4He Magnetometers at Ambient Temperature," IEEE Trans. Med. Imaging **38**(1), 90–98 (2019).
19. J. Rutkowski, W. Fourcault, F. Bertrand, U. Rossini, S. Gétin, S. Le Calvez, T. Jager, E. Herth, C. Gorecki, M. Le Prado, J. M. Léger, and S. Morales, "Towards a miniature atomic scalar magnetometer using a liquid crystal polarization rotator," Sens. Actuators, A **216**, 386–393 (2014).
20. F. D. Colegrove and P. A. Franken, "Optical Pumping of Helium in the $^3S_1$ Metastable State," Phys. Rev. **119**(2), 680–690 (1960).
21. E. Breschi and A. Weis, "Ground-state Hanle effect based on atomic alignment," Phys. Rev. A **86**(5), 053427 (2012).
22. A. Omont, "Irreducible components of the density matrix. Application to optical pumping," Prog. Quantum Electron. **5**, 69–138 (1977).
23. J. Osborne, J. Orton, O. Alem, and V. Shah, "Fully integrated, standalone zero field optically pumped magnetometer for biomagnetism," in *Steep Dispersion Engineering and Opto-Atomic Precision Metrology XI*, vol. 10548 (International Society for Optics and Photonics, 2018), p. 105481G.
24. G. Zhang, S. Huang, and Q. Lin, "Magnetoencephalography using a compact multichannel atomic magnetometer with pump-probe configuration," AIP Adv. **8**(12), 125028 (2018).
25. T. Karaulanov, I. Savukov, and Y. J. Kim, "Spin-exchange relaxation-free magnetometer with nearly parallel pump and probe beams," Meas. Sci. Technol. **27**(5), 055002 (2016).

Optics EXPRESS

26. A. Borna, T. R. Carter, J. D. Goldberg, A. P. Colombo, Y.-Y. Jau, C. Berry, J. McKay, J. Stephen, M. Weisend, and P. D. D. Schwindt, "A 20-channel magnetoencephalography system based on optically pumped magnetometers," Phys. Med. Biol. **62**(23), 8909–8923 (2017).
27. F. Beato and A. Palacios-Laloy, "Second-order effects in parametric-resonance magnetometers based on atomic alignment," EPJ Quantum Technol. **7**(1), 9–14 (2020).
28. F. Beato, E. Belorizky, E. Labyt, M. Le Prado, and A. Palacios-Laloy, "Theory of a 4He parametric-resonance magnetometer based on atomic alignment," Phys. Rev. A **98**(5), 053431 (2018).
29. J. Dupont-Roc, "Étude théorique de diverses résonances observables en champ nul sur des atomes ≪ habillés ≫ par des photons de radiofréquence," J. Phys. **32**(2-3), 135–144 (1971).
30. R. E. Slocum, "Advances in optically pumped He4 magnetometers : Resonance and nonresonance techniques," Rev. de Phys. Appl. **5**(1), 109–112 (1970).
31. O. Alem, K. L. Sauer, and M. V. Romalis, "Spin damping in an rf atomic magnetometer," Phys. Rev. A **87**(1), 013413 (2013).
32. D. Sheng, A. R. Perry, S. P. Krzyzewski, S. Geller, J. Kitching, and S. Knappe, "A microfabricated optically-pumped magnetic gradiometer," Appl. Phys. Lett. **110**(3), 031106 (2017).
33. R. Wyllie, "The development of a multichannel atomic magnetometer array for fetal magnetocardiography," Ph.D. thesis, University of Wisconsin-Madison (2012).
34. Z. J. DeLand, "Advances in fetal magnetocardiography using SERF atomic magnetometers," Ph.D. thesis, University of Wisconsin–Madison (2017).
35. H. B. Hui, D. Pantazis, S. L. Bressler, and R. M. Leahy, "Identifying true cortical interactions in meg using the nulling beamformer," NeuroImage **49**(4), 3161–3174 (2010).
36. M. Le Prado, F. Bertrand, S. Morales, and A. Palacios-Laloy, "Reseau de magnetometres vectoriels et procede associe de calibration des couplages entre magnetometres," French patent application FR3056761-B1 (2018).
37. J. Dupont-Roc, "Détermination par des méthodes optiques des trois composantes d'un champ magnétique très faible," Rev. de Phys. Appl. **5**(6), 853–864 (1970).
38. T. M. Tierney, N. Holmes, S. Mellor, J. D. López, G. Roberts, R. M. Hill, E. Boto, J. Leggett, V. Shah, M. J. Brookes, R. Bowtell, and G. R. Barnes, "Optically pumped magnetometers: From quantum origins to multi-channel magnetoencephalography," NeuroImage (2019).
39. G. Le Gal, G. Lieb, F. Beato, T. Jager, H. Gilles, and A. Palacios-Laloy, "Dual-Axis Hanle Magnetometer Based on Atomic Alignment with a Single Optical Access," Phys. Rev. Appl. **12**(6), 064010 (2019).